

---

# Simulated Annealing ABC with multiple summary statistics

---

**Carlo Albert**  
Swiss Federal Institute  
of Aquatic Science and Technology

**Simone Ulzega**  
Zurich University of Applied Sciences

**Simon Dirmeier**  
Swiss Data Science Center  
ETH Zurich

**Andreas Scheidegger**  
Swiss Federal Institute  
of Aquatic Science and Technology

**Alberto Bassi**  
Swiss Federal Institute  
of Aquatic Science and Technology  
ETH Zurich

**Antonietta Mira**  
Università della Svizzera italiana  
University of Insubria

## Abstract

Bayesian inference for stochastic models is often challenging because evaluating the likelihood function typically requires integrating over a large number of latent variables. However, if only few parameters need to be inferred, it can be more efficient to perform the inference based on a comparison of the observations with (a large number of) model simulations, in terms of only few summary statistics. In Machine Learning (ML), Simulation Based Inference (SBI) using neural density estimation is often considered superior to the traditional sampling-based approach known as Approximate Bayesian Computation (ABC). Here, we present a new set of ABC algorithms based on Simulated Annealing and demonstrate that they are competitive with ML approaches, whilst requiring much less hyper-parameter tuning. For the design of these sampling algorithms we draw intuition from non-equilibrium thermodynamics, where we associate each summary statistic with a state variable (energy) quantifying the distance to the observed value as well as a temperature that controls the degree to which the associated statistic contributes to the posterior. We derive an optimal annealing schedule on a Riemannian manifold of state variables based on a minimal entropy production principle. Our new algorithms generalize the established Simulated Annealing based ABC to multiple state variables and temperatures. In situations where the information-content is unevenly distributed among the summary statistics, this can greatly improve performance of the algorithm. Our method also allows monitoring the convergence of individual statistics, which is a great diagnostic tool in out-of-sample situations. We validate our approach on standard benchmark tasks from the SBI literature and a hard inference problem from solar physics and demonstrate that it is highly competitive with the state-of-the-art.

## 1 Introduction

Bayesian inference algorithms that require a large number of likelihood evaluations become impractical when this evaluation involves a very high dimensional integration, as is typically the case with stochastic models. *Simulation-based inference algorithms* (SBI) circumvent the evaluation of the

likelihood function and instead approximate the posterior based on a large number of simulated model outputs obtained with different sets of parameters. As the number of model parameters is typically much smaller than the output dimension, considering only a relatively small number of *summary statistics* of the output suffices for a good posterior approximation. Herein lies the efficiency gain of simulation-based inference algorithms.

There are two classes of simulation-based algorithms. The first one uses neural density estimators, Machine Learning (ML) models that attempt to learn either the posterior density or the likelihood directly. Simultaneously, they typically also attempt to learn a minimal set of near-sufficient summary statistics. The second one comprises algorithms that attempt to *sample* from an approximate posterior based on comparing simulated with observed summary statistics. Because this comparison typically involves a strictly positive tolerance introducing a layer of approximation, these sampling approaches are called *Approximate Bayes Computation* (ABC). While ML methods can be very fast, they often suffer from biases that are hard to control. Furthermore, they typically have a large number of hyper-parameters requiring non-trivial tuning. ABC algorithms, on the other hand, tend to be very simulation-intense, but their bias can be controlled by the tolerance between simulated and observed statistics. Furthermore, ABC algorithms based on *simulated annealing* (SABC, Albert et al. (2014); Albert (2015)) are largely self-tuning as they lower the tolerance adaptively during the course of the algorithm based on a *minimal entropy production* principle. One shortcoming of existing ABC algorithms is that the user needs to choose a metric on the space of summary statistics. This choice can greatly influence the efficiency of the algorithm. While standardizing the summary statistics with respect to the prior can balance their contribution to the acceptance probability to some extent, their prior distributions can still be very different. A large skewness of certain statistics, for instance, could mean that they are quickly losing their influence once the few "bad samples" have been removed during the course of the algorithm. The original SABC algorithm "rectifies" the user-defined metric such that it follows a uniform distribution under the prior. Here, we propose to rectify the univariate distances *individually*, for each summary statistic. We expect this to balance the contribution of different summary statistics to the acceptance probability of proposed moves throughout the algorithm. Furthermore, we propose a variant of SABC where each summary statistic comes with its own dynamic tolerance (or temperature). The rationale behind it is that more informative summary statistics are expected to converge faster: as they couple stronger to the parameters, they are expected to profit more from the convergence towards the posterior. Hence, the tolerances of the more informative summary statistics are expected to decay faster, and, in turn, lead to a faster convergence towards the true posterior.

Ideally, summary statistics should encode most of the information that is relevant for constraining the parameters while filtering out as much noise as possible. Such statistics can be found by means of ML models (e.g., Chen et al. (2021), Albert et al. (2022), Chen et al. (2023)). In practice, however, the information relevant for constraining the parameters will be distributed quite unevenly across the statistics, and might even change on the course of the annealing. To some extent, our algorithms can counter-balance this unevenness, and thus allow for an optimal extraction of information, for each model simulation. Furthermore, our method allows monitoring the convergence of each summary statistic individually. In cases where the observations are out-of-sample, this can help identify the features the model struggles to fit. Allowing those features to be less compliant with the observations by using individual temperatures can also improve robustness.

We benchmark our new SABC variants against an ABC variant that is not based on annealing, as well as state-of-the-art ML approaches, and show that they are generally competitive, and can be superior in hard cases. Finally, we apply them to a challenging real-world scenario, where their robustness becomes particularly evident.

## 2 Theory

Consider a stochastic model with intractable density  $f(\mathbf{x}|\boldsymbol{\theta})$  dependent on model parameters  $\boldsymbol{\theta}$ . We are given a low-dimensional vector of summary statistics,  $\mathbf{s}(\mathbf{x})$ , and write the derived joint prior distribution of statistics and parameters as  $f(\mathbf{s}, \boldsymbol{\theta}) = f(\mathbf{s}|\boldsymbol{\theta})f(\boldsymbol{\theta})$ . We are interested in the *posterior*, that is the joint prior conditioned on the summary statistics of observed data,  $f(\boldsymbol{\theta}|\mathbf{s}(\mathbf{x}_{obs}))$ . If we assume that the statistics are *sufficient*, this posterior will be identical to the full posterior conditioned on all the data,  $f(\boldsymbol{\theta}|\mathbf{x}_{obs})$ . However, we do not impose this requirement here.

SABC algorithms start with a population of particles drawn from the joint prior  $f(\mathbf{s}, \boldsymbol{\theta})$ , and iteratively update these particles drawing from the transition probability

$$q(\mathbf{s}', \boldsymbol{\theta}' | \mathbf{s}, \boldsymbol{\theta}) := k(\boldsymbol{\theta}' | \boldsymbol{\theta}) f(\mathbf{s}' | \boldsymbol{\theta}') \min(1, \exp[-\beta^e(\rho(\mathbf{s}') - \rho(\mathbf{s}))] f(\boldsymbol{\theta}') / f(\boldsymbol{\theta})) + \delta(\boldsymbol{\theta} - \boldsymbol{\theta}') \delta(\mathbf{s} - \mathbf{s}') r(\mathbf{s}, \boldsymbol{\theta}), \quad (1)$$

with appropriate rejection probability  $r(\mathbf{s}, \boldsymbol{\theta})$ . That is, we suggest a new particle position by first jumping randomly in parameter space according to the symmetric distribution  $k(\boldsymbol{\theta}' | \boldsymbol{\theta})$ , then we *simulate* a new model output  $\mathbf{x}' \sim f(\mathbf{x}' | \boldsymbol{\theta}')$  and calculate its summary statistics  $\mathbf{s}' = \mathbf{s}(\mathbf{x}')$ . The proposal particle is then accepted with the usual Metropolis probability determined by the ratio of the prior probabilities for the parameters and the difference of the distances of the simulated statistics to the target  $\mathbf{s}_{obs}$  measured by a user-specified metric  $\rho(\cdot)$ . The inverse temperature  $\beta^e$  is gradually increased thus forcing the population to be more and more compliant with the data. It has been shown in Albert et al. (2014) that convergence to the posterior  $f(\boldsymbol{\theta} | \mathbf{s}_{obs})$  is ascertained upon sufficiently slow annealing (according to a power law depending on the number of summary statistics). In practice, we prefer to use an annealing schedule that adapts the temperature based on the current average distance of the particles from the target. The adaptive SABC algorithm reparameterizes the distance function  $\rho(\cdot)$  using an *energy* function in such a way that a minimal entropy production principle can be invoked for an optimal annealing Albert et al. (2014).

If we have more than one summary statistic, it can be challenging to come up with a metric  $\rho(\mathbf{s})$  that balances their contribution to the Metropolis probability throughout the algorithm. The solution we propose here is to introduce a separate energy, for each statistic. First, we replace the statistics,  $s^i$ ,  $i = 1, \dots, n$ , by their distances,  $\rho^i = \rho^i(s^i)$ , to the observed statistics  $s_{obs}^i$ . Then, we re-parameterize those distances by means of their cdfs with respect to the prior marginals  $f(\rho^i)$  and define the new energy coordinates,  $u^i$ , as

$$u^i(\rho^i) := \int_{\tilde{\rho}^i < \rho^i} f(\tilde{\rho}^i) d\tilde{\rho}^i. \quad (2)$$

This choice will allow us to easily derive the temperatures from the observed energies (see eq. 20 below). Algorithmically, this reparameterization can be approximately performed during the initialization of the algorithm when a large prior sample of parameters and associated summary statistics is drawn. We introduce a separate temperature,  $\beta_i^e$  ( $i = 1, \dots, n$ ), for each summary statistic and apply the new update rule

$$q(\mathbf{u}', \boldsymbol{\theta}' | \mathbf{u}, \boldsymbol{\theta}) := k(\boldsymbol{\theta}' | \boldsymbol{\theta}) f(\mathbf{u}' | \boldsymbol{\theta}') \min \left( 1, \exp \left[ - \sum_i \beta_i^e (u'^i - u^i) \right] \frac{f(\boldsymbol{\theta}')}{f(\boldsymbol{\theta})} \right) + \delta(\boldsymbol{\theta} - \boldsymbol{\theta}') \delta(\mathbf{u} - \mathbf{u}') r(\mathbf{u}, \boldsymbol{\theta}) \quad (3)$$

(sequentially or in parallel) to a large number of particles. If the annealing is not too fast w.r.t. the mixing in parameter space, we can make the *endoreversibility assumption* according to which the population approximates, at any time, the distribution

$$\pi_{\beta}(\mathbf{u}, \boldsymbol{\theta}) = Z^{-1}(\beta) f(\mathbf{u}, \boldsymbol{\theta}) \exp \left[ - \sum_i \beta_i u^i \right], \quad (4)$$

where the inverse *internal* temperatures,  $\beta_i$ , are slightly smaller than the respective external ones  $\beta_i^e$ .

The adaptive annealing scheme we apply is based on the premise of *minimal entropy production*. If the number of particles is sufficiently large, and the number of particles that get updated in a single time-step of the algorithm is sufficiently small, we can assume the observable *energy densities*

$$\mathbf{U}(\beta) := \int \mathbf{u} \pi_{\beta}(\mathbf{u}, \boldsymbol{\theta}) d\mathbf{u} d\boldsymbol{\theta} \quad (5)$$

to be continuously varying in time. Under the endoreversibility assumption, the entropy production rate is then given by the product of thermodynamic fluxes and forces, as

$$\dot{S}_{prod} = \sum_i \dot{U}^i F_i, \quad (6)$$

where  $F_i := \beta_i^e - \beta_i$  (see Albert et al. (2014) and references therein for the thermodynamic background). Using (3) through (5) and the *master equation* describing the dynamics of (4) we derive the fluxes as Albert et al. (2014)

$$\begin{aligned} \dot{\mathbf{U}}(\beta, \beta^e) = Z^{-1}(\beta) \int (\mathbf{u} - \mathbf{u}') k(\boldsymbol{\theta}|\boldsymbol{\theta}') f(\mathbf{u}|\boldsymbol{\theta}) f(\mathbf{u}', \boldsymbol{\theta}') \\ \times \min \left( 1, \exp \left[ - \sum_i \beta_i^e (u^i - u'^i) \right] \frac{f(\boldsymbol{\theta})}{f(\boldsymbol{\theta}')} \right) \exp \left[ - \sum_i \beta_i u'^i \right] d\mathbf{u} d\boldsymbol{\theta} d\mathbf{u}' d\boldsymbol{\theta}'. \end{aligned} \quad (7)$$

We assume that the annealing is slow enough to warrant the linearity assumption

$$\dot{\mathbf{U}} \approx L(\mathbf{U}) \mathbf{F}. \quad (8)$$

Minimal entropy production, for fixed initial and final energies (the final energies being  $\mathbf{U} = 0$ ) means that the system needs to follow a *geodesic curve*, w.r.t. the metric defined by the negative inverse *Onsager matrix*:  $g_{ij}(\mathbf{U}) := -L_{ij}^{-1}(\mathbf{U})$ . In general, this metric is intractable. Therefore, in order to come up with a first order approximation, we make three assumptions that are at best approximately satisfied. We assume that (i) the prior is not very informative ( $f(\boldsymbol{\theta}) \approx 1$ ), (ii) the jump distribution is rather broad ( $k(\boldsymbol{\theta}|\boldsymbol{\theta}') \approx 1$ ), and (iii) the summary statistics should be such that, at least for small values of  $\mathbf{u}$ ,  $f(\mathbf{u}) \approx \text{const}$ . Assumption (i) is reasonable. Indeed, if the prior is very informative, gradually lowering the tolerance (such as in sequential Monte Carlo (SMC)-ABC Beaumont et al. (2009) or SABC) might even be detrimental and one might be better off with a simple rejection ABC. Assumption (ii) means that mixing should be sufficiently fast. This is indeed necessary for the endoreversibility condition to be valid. Assumption (iii) requires that the summary statistics are not overly correlated and that the prior is sufficiently broad relative to the posterior—both of which are reasonable conditions. Under these assumptions, the parameters can trivially be integrated out, and (7) is approximated by the integral

$$\dot{\mathbf{U}} \approx c_0 \int (\mathbf{u} - \mathbf{u}') \min \left( 1, \exp \left[ - \sum_i \beta_i^e (u^i - u'^i) \right] \right) \times \exp \left[ - \sum_i \beta_i u'^i \right] \prod_i \beta_i du^i du'^i, \quad (9)$$

where  $c_0$  is a constant that does not strongly depend on the number of summary statistics. Introducing coordinates  $u_{\pm}^i = u^i \pm u'^i$ , and assuming that  $\beta_i \gg 1$ , we find that

$$\dot{\mathbf{U}} \approx c_0 \int \mathbf{u}_- \min \left( 1, \exp \left[ - \sum_i \beta_i^e u_-^i \right] \right) \prod_i \min \left( 1, \exp \left[ \sum_j \beta_j u_-^j \right] \right) du_-^i. \quad (10)$$

Expanding the r.h.s. around  $\beta_e = \beta$ , yields (see Appendix A for details)

$$\begin{aligned} L^{ij}(\mathbf{U}) &\approx -c_0 \int u_-^i u_-^j \chi \left( \sum_k \beta_k u_-^k \right) \prod_l \min \left( 1, \exp \left[ - \sum_k \beta_k u_-^k \right] \right) du_-^l \\ &= -c_n \left( \prod_k U^k \right) U^i U^j (-1 + \delta^{ij}(n+1)), \end{aligned} \quad (11)$$

where the coefficients  $c_n = c_0(2n+2)!/((n+1)!(n+2)!)$  are proportional to the *Catalan numbers*. Inverting this matrix yields the metric

$$g_{ij}(\mathbf{U}) = \frac{1}{c_n(n+1)} \frac{1}{U^i U^j} \prod_k (U^k)^{-1} (\delta_{ij} + 1). \quad (12)$$

The change of coordinates  $P^i = \ln U^i$  renders this metric *conformally flat*:

$$g_{ij}(\mathbf{P}) = c_n^{-1} e^{-\Phi(\mathbf{P})} \eta_{ij}, \quad (13)$$

with  $\Phi(\mathbf{P}) = \sum_i P^i$  and  $\eta_{ij} = (\delta_{ij} + 1)/(n+1)$ . In order to find the geodesics we need to calculate the *Christoffel symbols*<sup>1</sup>

$$\Gamma_{jk}^i = \frac{1}{2} g^{il} (g_{lj,k} + g_{lk,j} - g_{jk,l}) = \frac{1}{2} (-\delta_j^i - \delta_k^i + \eta_{jk}). \quad (14)$$

<sup>1</sup>Here and in the following, we adopt the Einstein convention automatically summing over repeated co- and contravariant indices.

Due to symmetry, the simplest geodesic curves in  $\mathbf{P}$ -space are straight lines with slope one. Setting  $\dot{P}^i = \dot{P}^j$ , for all  $i, j$ , the geodesic equation simplifies to

$$\ddot{P}^i = -\Gamma_{jk}^i \dot{P}^j \dot{P}^k = \frac{n}{2} (\dot{P}^i)^2. \quad (15)$$

Thus,  $P^i(t) = P_0^i - (2/n) \ln(vnt/2 + 1)$ , where  $v$  denotes the velocity, and which reads in  $\mathbf{U}$  space as

$$U^i(t) = U_0^i \left( \frac{vn}{2} t + 1 \right)^{-2/n}. \quad (16)$$

Hence,

$$\dot{U}^i(t) = -v(U_0^i)^{-n/2} (U^i(t))^{1+n/2}, \quad (17)$$

from which we see that geodesics are straight lines ending at  $\mathbf{U} = 0$ . Finally, we need to calculate the thermodynamic force, using (12) and (17). Setting the initial conditions to  $U_0^i = 1$ , we get

$$F_i(\mathbf{U}) = -g_{ij}(\mathbf{U}) \dot{U}^j = v \frac{1 + \sum_j (U^j/U^i)^{n/2}}{c_n(n+1)(U^i)^{1+n/2} \prod_j (U^j/U^i)}, \quad (18)$$

from which we get the adaptive annealing schedule

$$\beta_i^e(\mathbf{U}) = \beta_i(U^i) + v \frac{1 + \sum_j (U^j/U^i)^{n/2}}{c_n(n+1)(U^i)^{1+n/2} \prod_j (U^j/U^i)}. \quad (19)$$

Note that the approximation  $\beta_i \approx 1/U^i$  is valid only for  $U^i \ll 1$ . However, at the beginning of the algorithm,  $U^i = 1/2$ . Including the boundary condition that  $u^i \leq 1$ , we get the relation

$$U^i = \frac{1 - e^{-\beta_i(1 + \beta_i)}}{\beta_i(1 - e^{-\beta_i})}, \quad (20)$$

which yields  $U^i = 1/2$ , for  $\beta_i = 0$ , as it ought to be. We therefore suggest to numerically solve eq. (20) for determining the current temperatures  $\beta_i(U^i)$ .

If the trajectory did stay on the diagonal, eq. (19) would simplify to  $\beta_i^e(\mathbf{U}) = \beta_i(U^i) + (v/c_n)(U^i)^{1+n/2}$ . As Assumptions (i) through (iii) above are generally not satisfied, trajectories will deviate from the diagonal. In fact, it can be desirable to allow certain statistics to converge faster than others, as these are typically the statistics that contain more parameter-related information (see next section). However, this feature can also lead to an instability in certain cases. Therefore, we also offer a variant of the algorithm where all  $\beta_i^e$  are set equal, which forces the trajectory to be closer to the diagonal. In this case, we suggest to resort to the original annealing schedule proposed in Albert et al. (2014). The only difference is that the user does not have to aggregate the distances associated with different summary statistics, but the algorithm calculates an energy for each individual distance and then adds them up. We call this latter variant *SABC single*, and the former *SABC multi*.

## 3 Experiments

### 3.1 Benchmark tasks

We evaluate the introduced variants of SABC across four benchmark tasks. Three are standard benchmarks from the SBI literature: the two moons example, a hyperboloid model and a mixture model Lueckmann et al. (2021). The forth is a Gaussian mixture model with distractors, mimicking the presence of uninformative summary statistics. When sampling its posterior with SABC, both the informative as well as the uninformative components of proposed particles have a decreasing chance of getting accepted as they are zeroing in on the observed values. However, the informative components have an advantage as they profit from the convergence of the parameters towards the posterior. This allows them to decay faster than the uninformative statistics when equipped with their own tolerances, and exemplifies the advantage of using multiple temperatures. More details on the models can be found in Appendix B.1.

To systematically evaluate the variance of each estimator, we repeat the four benchmark evaluations using five different random number seeds. For each seed, we compute ground-truth posterior samples as described in Appendix B.2 and compare them to the approximate posteriors from each method. To

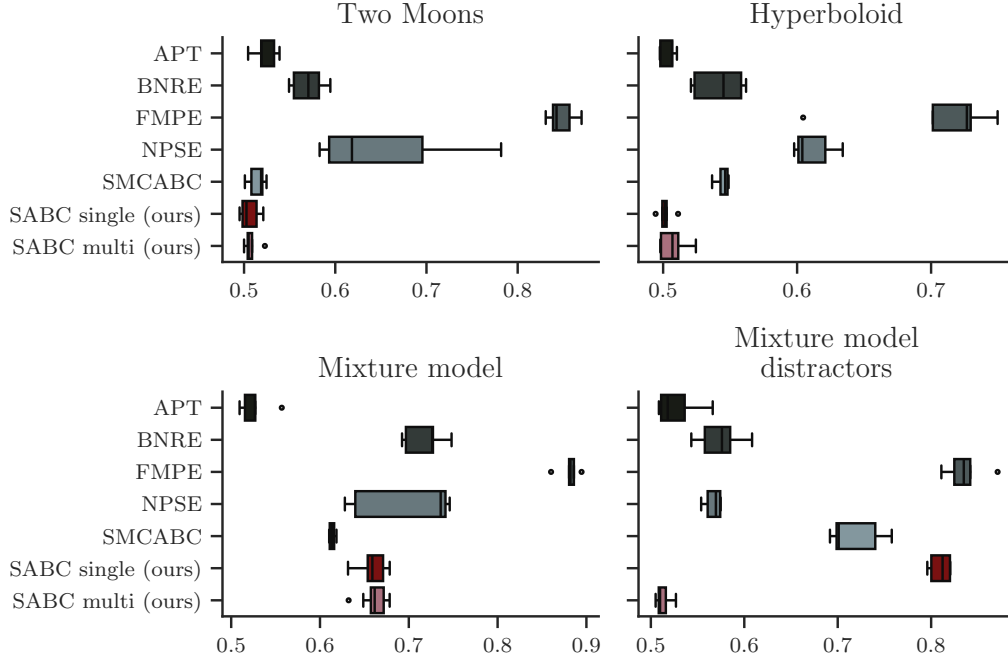


Figure 1: SABC performance on benchmark tasks using a C2ST metric (lower is better, ideal is 0.5).

evaluate the performance of each method, we compute classifier two-sample tests (C2ST; Lopez-Paz and Oquab (2017)), maximum mean discrepancy (MMD; (Sutherland et al., 2017)), and the recently suggested H-min distance (Zhao et al., 2022; Dirmeier et al., 2023).

We compare SABC (single and multi) against multiple baseline methods: automatic posterior transformation (APT, Greenberg et al. (2019)), balanced neural ratio estimation (BNRE, Delaunoy et al. (2022)), flow matching posterior estimation (FMPE, Wildberger et al. (2023)), neural posterior score estimation (NPSE, Sharrock et al. (2024)), and sequential Monte Carlo approximate Bayesian computation (SMC-ABC, Beaumont et al. (2009)). We refer to Appendix B.2 for experimental and implementation details.

Among the four benchmark evaluations, SABC either outperforms or is on par with the state-of-the-art (Fig. 1 and Fig. 6 in the Appendix) except for the mixture model example, where APT shows to have a strong advantage. As expected using multiple temperatures is also very beneficial in the presence of distractors (see the bottom right panel in Fig. 1 as well as the decay of the individual distances in Fig. 10).

Qualitatively, we found the inferences of SABC to also be on-par with APT (compare the posteriors in Fig. 2 and Appendix B.3.2).

### 3.2 Solar Dynamo

We also evaluate SABC on a real-world example from the solar physics literature, namely a stochastic delay differential equation model describing the dynamics of the solar magnetic field strength  $B(t)$  (see Appendix C.1). We make use of the official observed sunspot number (SN) record from Clette and Lefèvre (2015), a proxy for the solar magnetic field, for which we compute summary statistics consisting of a set of 20 frequency components (Fig. 3).

We compare SABC (*single* outperformed *multi* on this task) against the two sequential posterior estimation methods APT/SNPE-C and SNLE (Greenberg et al., 2019; Papamakarios et al., 2019), since they, in our experiments, demonstrated the best performance on this task in comparison to more recent methods (data not shown, experimental details can be found in Appendix C.2). Despite significant practical and computational effort, such as the evaluation of multiple density estimation

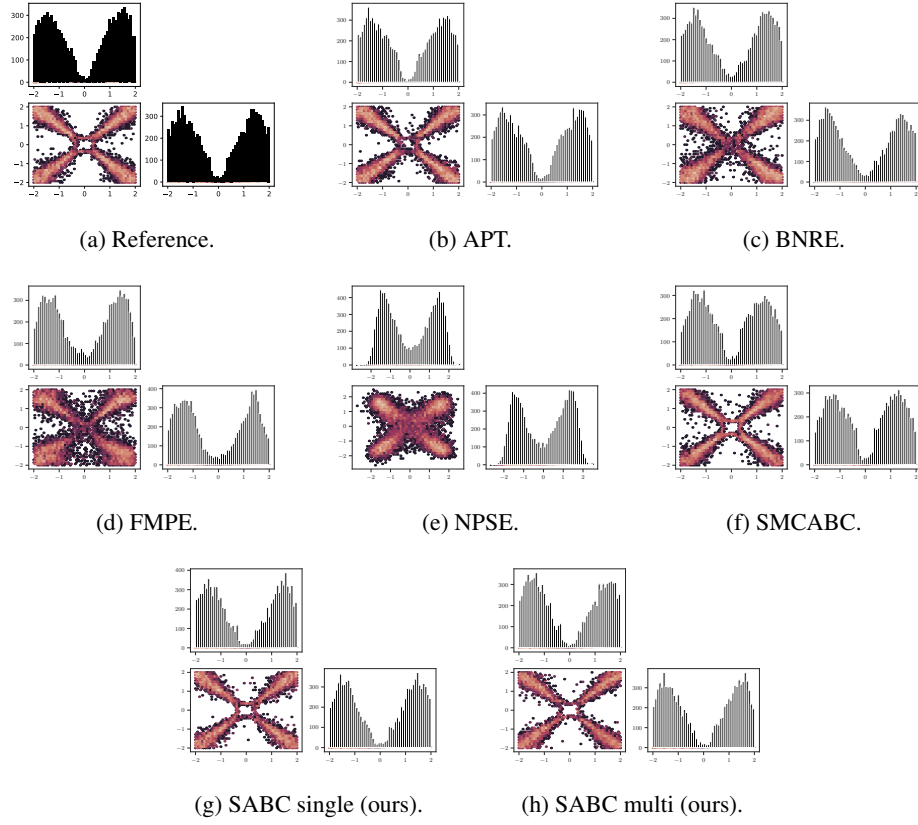


Figure 2: Posterior distributions for the hyperboloid example using an arbitrary seed.

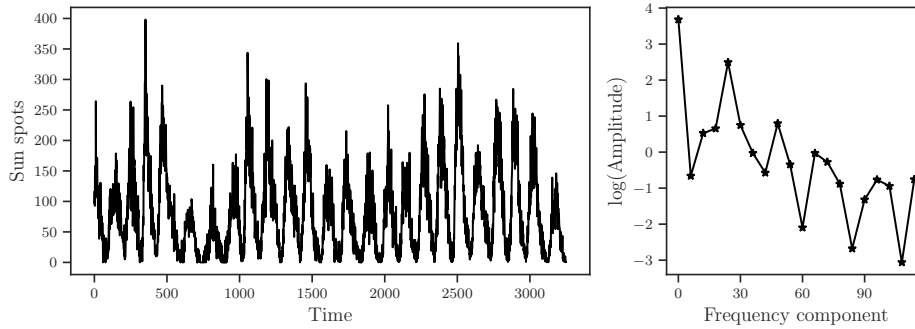


Figure 3: The SN record. The sunspots dataset consists of 3251 monthly observations measured from 1749 to 2019 having a characteristic period of about 11 years (left). The summary statistics consist of 20 Fast Fourier transform components of different frequencies.

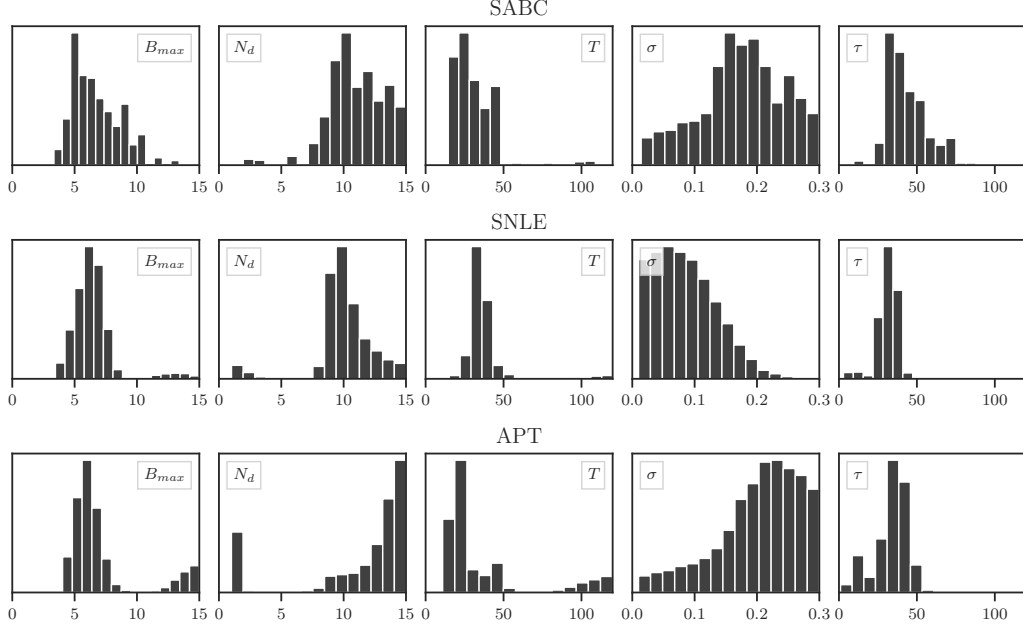


Figure 4: Solar dynamo posterior distributions of SABC, SNLE and APT.

and embedding network architectures, and the fact that it was previously shown that neural SBI methods scale easily to higher data or parameter dimensions, we were not able to infer meaningful posterior distributions when applying APT and SNLE to the raw data. As a consequence, we use the same summary statistics for APT and SNLE that we also use for SABC (here, we evaluated linear, MLP and RNN-based embedding networks and found that a linear projection yielded the best posterior predictive distributions, see eq. (21) below).

The posteriors achieved with the three methods are quite similar (Fig. 4 and 11 through 13 in Appendix C.3), demonstrating the competitiveness of SABC even on higher-dimensional problems. The results are also in line with expectations from domain knowledge Ulzega et al. (2025).

The solar dynamo model does not admit a tractable likelihood function and the previously used metrics cannot be computed. We instead evaluate the inferred posterior comparing the posterior predictive distribution (PPD),

$$f(s(\mathbf{x})|s(\mathbf{x}_{obs})) = \int f(s(\mathbf{x})|\boldsymbol{\theta})f(\boldsymbol{\theta}|s(\mathbf{x}_{obs}))d\boldsymbol{\theta}, \quad (21)$$

to the calibration data. Fig. 5 shows that SABC and APT appear to agree somewhat better with the data than SNLE.

As a more challenging out-of-sample problem, we also calibrated the same dynamo model to a very different (and much longer) dataset: a reconstruction of sunspot numbers from  $^{14}\text{C}$  records retrieved from tree rings Usoskin et al. (2021). Fig. 16 shows that this dataset is much more out-of-sample than the directly observed sunspots, with low-frequency features and artefacts such as negative sunspot numbers that are not represented in our model. Despite these shortcomings, SABC appears to do a decent job in inferring the model parameters, which are remarkably consistent with the ones derived from directly observed sunspots (see Fig. 14). APT and SNLE, on the other hand, produce posteriors that are not quite in line with previous findings and PPDs that indicate difficulties in fitting the main frequency peak (Fig. 15), corroborating the known difficulty of these methods to deal with out-of-sample situations.

It is interesting to compare the decay of the energies (rectified distances to the observed Fourier components) of the two datasets (Fig. 17): While the energies for the sunspots decay more or less in unison, the  $^{14}\text{C}$  data exhibits two trailing energies. One of them is associated with one of the low-frequency components of the data the model is not able to reproduce very well, and the other



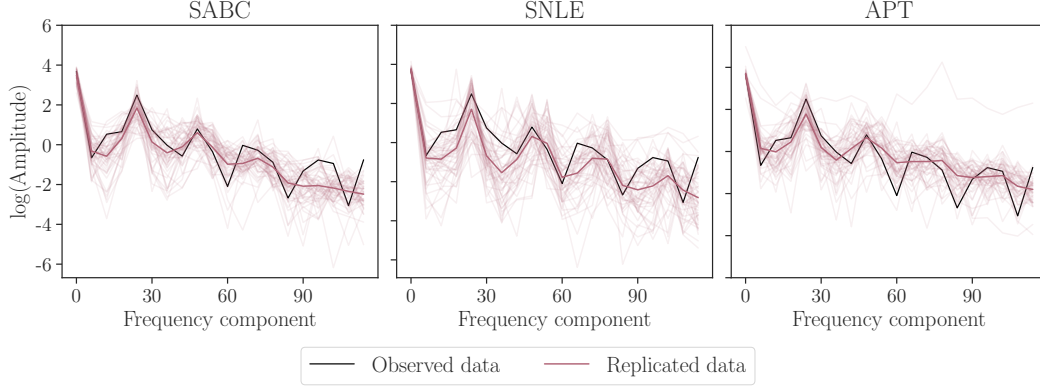


Figure 5: SABC posterior predictive distributions.

one is associated with the main (roughly 11y) cycle of the data. As this cycle is modulated quite heavily, both in terms of frequency and amplitude, the model appears to have difficulties reproducing it accurately.

## 4 Conclusions

With this paper, we want to make a case for ABC as a viable, and sometimes even superior alternative to neural density estimators (ML methods). Whilst ML methods are generally very efficient, they are not guaranteed to converge. ABC methods, at least in theory, can approximate the true posterior arbitrarily well upon sufficient investment of compute. Furthermore, the distances to the observations of the last accepted parameter proposals give us a level of trust in the approximation of the posterior ML methods cannot provide. In scientific applications, where a reliable quantification of uncertainty is important, this is a strong argument in favor of ABC. In contrast to ML, ABC methods, in particular the SABC variants, are also much easier to tune.

However, when more than one summary statistic is to be matched, the efficiency of SABC strongly depends on the chosen metric. Here, we suggest to use separate energies (rectified distances) and possibly also separate temperatures (tolerances), which comes with a number of advantages:

- It simplifies the tuning even further, as the user does not need to find an appropriate metric. The use of separate energies balances the contribution of the different summary statistics automatically throughout the algorithm, while the use of separate temperatures can allow more informative statistics to converge faster.
- It provides a diagnostic tool: The speed with which the individual energies diminish allows us to analyze which features (summary statistics) are well matched and which not. This knowledge can then be used to either improve the model or ignore certain features of the data.
- It makes the algorithm more robust: Allowing hard-to-match features to comply less stringently with the data (i.e. to converge slower) can be beneficial in out-of-sample situations.

We have demonstrated the competitiveness and advantages of our new SABC variants in terms of benchmarks and a hard inference problem from solar physics.

The main limitation of our method (and this pertains to all ABC methods) is that it typically requires a very large number of model simulations. For simulators that take minutes or longer to run, a faster surrogate model might be required to run ABC. Our implementation of SABC single is more or less identical with the original SABC algorithm (except for the use of particle interactions instead of a random walk in parameter space). However, we expect that summing up energies will beat user-defined metrics on the space of summary statistics in most cases. SABC multi showed promising results in our benchmark tests, especially when adding uninformative statistics. However, our experience with this variant in real-world applications is still limited.

## Acknowledgement

This work has been supported by the Swiss National Science Foundation (Grant N<sup>o</sup> 208249).

## References

- Albert, C. (2015). A Simulated Annealing Approach to Bayesian Inference. *arXiv:1509.05315*.
- Albert, C., Ferriz-Mas, A., Gaia, F., and Ulzega, S. (2021). Can Stochastic Resonance explain recurrence of Grand Minima? *The Astrophysical Journal Letters*, 916(2):L9.
- Albert, C., Künsch, H.-R., and Scheidegger, A. (2014). A Simulated Annealing Approach to Approximate Bayes Computations. *Stat. Comput.*, 25(6):1217–1232.
- Albert, C., Ulzega, S., Ozdemir, F., Perez-Cruz, F., and Mira, A. (2022). Learning summary statistics for Bayesian inference with Autoencoders. *SciPost Physics Core*, 5(3):043.
- Beaumont, M. A., Cornuet, J., Marin, J., and Robert, C. P. (2009). Adaptive approximate Bayesian computation. *Biometrika*, 96(4):983–990.
- Chen, Y., Gutmann, M. U., and Weller, A. (2023). Is learning summary statistics necessary for likelihood-free inference? In *International Conference on Machine Learning*.
- Chen, Y., Zhang, D., Gutmann, M., Courville, A., and Zhu, Z. (2021). Neural approximate sufficient statistics for implicit models. In *International Conference on Learning Representations*.
- Clette, F. and Lefèvre, L. (2015). Silso sunspot number v2.0. <https://doi.org/10.24414/qnza-ac80>. Published by WDC SILSO - Royal Observatory of Belgium (ROB).
- Delaunoy, A., Hermans, J., Rozet, F., Wehenkel, A., and Louppe, G. (2022). Towards reliable simulation-based inference with balanced neural ratio estimation. In *Advances in Neural Information Processing Systems*.
- Dirmeier, S., Albert, C., and Perez-Cruz, F. (2023). Simulation-based inference using surjective sequential neural likelihood estimation. *arXiv preprint arXiv:2308.01054*.
- Dirmeier, S., Ulzega, S., Mira, A., and Albert, C. (2024). Simulation-based inference with the Python package sbijax. *arXiv preprint arXiv:2409.19435*.
- Durkan, C., Bekasov, A., Murray, I., and Papamakarios, G. (2019). Neural spline flows. In *Advances in Neural Information Processing Systems*.
- Forbes, F., Nguyen, H. D., Nguyen, T., and Arbel, J. (2022). Summary statistics and discrepancy measures for approximate Bayesian computation via surrogate posteriors. *Statistics and Computing*, 32(5):85.
- Goodman, J. and Weare, J. (2010). Ensemble samplers with affine invariance. *Communications in applied mathematics and computational science*, 5(1):65–80.
- Greenberg, D., Nonnenmacher, M., and Macke, J. (2019). Automatic posterior transformation for likelihood-free inference. In *Proceedings of the 36th International Conference on Machine Learning*.
- Köster, J. and Rahmann, S. (2012). Snakemake—a scalable bioinformatics workflow engine. *Bioinformatics*, 28(19):2520–2522.
- Lopez-Paz, D. and Oquab, M. (2017). Revisiting classifier two-sample tests. In *International Conference on Learning Representations*.
- Lueckmann, J.-M., Boelts, J., Greenberg, D., Goncalves, P., and Macke, J. (2021). Benchmarking simulation-based inference. In *Proceedings of the 24th International Conference on Artificial Intelligence and Statistics*.
- Papamakarios, G., Pavlakou, T., and Murray, I. (2017). Masked autoregressive flow for density estimation. In *Advances in Neural Information Processing Systems*.

- Papamakarios, G., Sterratt, D., and Murray, I. (2019). Sequential neural likelihood: Fast likelihood-free inference with autoregressive flows. In *The 22nd International Conference on Artificial Intelligence and Statistics*.
- Sharrock, L., Simons, J., Liu, S., and Beaumont, M. (2024). Sequential neural score estimation: Likelihood-free inference with conditional score based diffusion models. In *Forty-first International Conference on Machine Learning*.
- Sutherland, D. J., Tung, H.-Y., Strathmann, H., De, S., Ramdas, A., Smola, A., and Gretton, A. (2017). Generative models and model criticism via optimized maximum mean discrepancy. In *International Conference on Learning Representations*.
- Tejero-Cantero, A., Boelts, J., Deistler, M., Lueckmann, J.-M., Durkan, C., Gonçalves, P. J., Greenberg, D. S., and Macke, J. H. (2020). sbi: A toolkit for simulation-based inference. *Journal of Open Source Software*, 5(52):2505.
- Ter Braak, C. (2006). A Markov Chain Monte Carlo version of the genetic algorithm differential evolution: easy Bayesian computing for real parameter spaces. *Statistics and Computing*, 16(3):239–249.
- Tong, A., Fatras, K., Malkin, N., Huguet, G., Zhang, Y., Rector-Brooks, J., Wolf, G., and Bengio, Y. (2024). Improving and generalizing flow-based generative models with minibatch optimal transport. *Transactions on Machine Learning Research*.
- Ulzega, S., Beer, J., Ferriz-Mas, A., Dirmeier, S., and Albert, C. (2025). Shedding light on the solar dynamo using data-driven Bayesian parameter inference. *in preparation*.
- Usoskin, I., Solanki, S. K., Krivova, N. A., Hofer, B., Kovaltsov, G., Wacker, L., Brehm, N., and Kromer, B. (2021). Solar cyclic activity over the last millennium reconstructed from annual 14C data. *Astronomy & Astrophysics*, 649:A141.
- Wildberger, J. B., Dax, M., Buchholz, S., Green, S. R., Macke, J. H., and Schölkopf, B. (2023). Flow matching for scalable simulation-based inference. In *Thirty-seventh Conference on Neural Information Processing Systems*.
- Wilmot-Smith, A., Nandy, D., Hornig, G., and Martens, P. (2006). A time delay model for solar and stellar dynamos. *The Astrophysical Journal*, 652(1):696.
- Zhao, S., Sinha, A., He, Y., Perreault, A., Song, J., and Ermon, S. (2022). Comparing distributions by measuring differences that affect decision making. In *International Conference on Learning Representations*.

## A Proof of Equation 11

After changing variables  $y_i := \beta_i u_-^i$ , we are left to prove the following integral:

$$L_n^{ij} := \int y_i y_j \theta \left( \sum_{k=1}^n y_k \right) \prod_{k=1}^n \min(1, e^{-y_k}) dy_k = c_n (-1 + \delta^{ij} (n+1)) , \quad (22)$$

where  $\theta(\cdot)$  is the Heaviside function and  $c_n = (2n+2)!/((n+1)!(n+2)!)$  are proportional to the Catalan numbers (here we re-define  $c_n$  from the main text by dividing by  $c_0$ ). Convergence is guaranteed by the Heaviside function constraint.

Due to symmetry, all the diagonal terms  $L_n^{ii}$ , for  $i = 1, \dots, n$ , are equal, and so are all the  $n(n-1)/2$  off-diagonal terms  $L_n^{ij}$  with  $i \neq j$ . Therefore, we only need to consider the following two terms as function of  $n$ :

$$Q_n := \int y_1^2 \theta \left( \sum_{k=1}^n y_k \right) \prod_{k=1}^n \min(1, e^{-y_k}) dy_k \quad (23)$$

$$M_n := \int y_1 y_2 \theta \left( \sum_{k=1}^n y_k \right) \prod_{k=1}^n \min(1, e^{-y_k}) dy_k . \quad (24)$$

In order to prove eq. (22) we prove  $Q_n = nc_n$  and  $M_n = -c_n$  by induction. It is easy to verify that:

$$Q_1 = \int_0^\infty y^2 e^{-y} dy = 2 = c_1 , \quad (25)$$

and

$$\begin{aligned} M_2 &= \int_{y_1+y_2>0} y_1 y_2 \min(1, e^{-y_1}) \min(1, e^{-y_2}) dy_1 dy_2 = \\ &= \int y_1 \min(1, e^{-y_1}) dy_1 \int_{y_2>-y_1} y_2 \min(1, e^{-y_2}) dy_2 = \\ &= \int y_1 \min(1, e^{-y_1}) dy_1 \left\{ \theta(y_1) \left( \int_0^\infty y_2 e^{-y_2} dy_2 + \int_{-y_1}^0 y_2 dy_2 \right) \right. \\ &\quad \left. + \theta(-y_1) \int_{-y_1}^\infty y_2 e^{-y_2} dy_2 \right\} = \\ &= \int y_1 \min(1, e^{-y_1}) dy_1 \left\{ \theta(y_1) (1 - y_1^2/2) + \theta(-y_1) (1 - y_1) e^{y_1} \right\} = \\ &= \int_0^\infty y_1 \left( 1 - \frac{y_1^2}{2} \right) e^{-y_1} dy_1 + \int_{-\infty}^0 y_1 (1 - y_1) e^{y_1} dy_1 = -5 = -c_2 . \quad (26) \end{aligned}$$

Now, let us solve  $Q_n$  by induction. We have for  $n > 1$ :

$$\begin{aligned} Q_{n+1} &:= \int y_1^2 \theta \left( \sum_{k=1}^{n+1} y_k \right) \prod_{k=1}^{n+1} \min(1, e^{-y_k}) dy_k = \\ &= \int y_1^2 \theta \left( \sum_{k=1}^n y_k + y_{n+1} \right) \prod_{k=1}^n \min(1, e^{-y_k}) dy_k \min(1, e^{-y_{n+1}}) dy_{n+1} . \quad (27) \end{aligned}$$

Given the theta constraint, we can split the integral into three integration regions :

$$\begin{aligned}
Q_{n+1} &= \int y_1^2 \theta\left(\sum_{k=1}^n y_k\right) \prod_{k=1}^n \min(1, e^{-y_k}) dy_k \int_0^\infty e^{-y_{n+1}} dy_{n+1} + \\
&\quad + \int y_1^2 \theta\left(\sum_{k=1}^n y_k\right) \prod_{k=1}^n \min(1, e^{-y_k}) dy_k \int_{-\sum_{k=1}^n y_k}^0 dy_{n+1} + \\
&\quad + \int y_1^2 \theta\left(-\sum_{k=1}^n y_k\right) \prod_{k=1}^n \min(1, e^{-y_k}) dy_k \int_{-\sum_{k=1}^n y_k}^\infty e^{-y_{n+1}} dy_{n+1} = \\
&= Q_n + \int y_1^2 \left(\sum_{k=1}^n y_k\right) \theta\left(\sum_{k=1}^n y_k\right) \prod_{k=1}^n \min(1, e^{-y_k}) dy_k + \\
&\quad + \int y_1^2 \theta\left(-\sum_{k=1}^n y_k\right) \prod_{k=1}^n \min(1, e^{-y_k}) \prod_{k=1}^n e^{y_k} dy_k = \\
&= 2Q_n + \sum_{k=1}^n \int y_1^2 y_k \theta\left(\sum_{k=1}^n y_k\right) \prod_{k=1}^n \min(1, e^{-y_k}) dy_k . \quad (28)
\end{aligned}$$

Similarly:

$$M_{n+1} = 2M_n + \sum_{k=1}^n \int y_1 y_2 y_k \theta\left(\sum_{k=1}^n y_k\right) \prod_{k=1}^n \min(1, e^{-y_k}) dy_k . \quad (29)$$

We introduce the linear and zeroth order terms

$$O_n := \int \theta\left(\sum_{k=1}^n y_k\right) \prod_{k=1}^n \min(1, e^{-y_k}) dy_k , \quad (30)$$

$$L_n := \int y_1 \theta\left(\sum_{k=1}^n y_k\right) \prod_{k=1}^n \min(1, e^{-y_k}) dy_k . \quad (31)$$

and the  $n$  dimensional measure

$$dY_n := \prod_{k=1}^n \min(1, e^{-y_k}) dy_k . \quad (32)$$

Then

$$\begin{aligned}
O_{n+1} &= \int dY_{n+1} \theta\left(\sum_{k=1}^{n+1} y_k\right) = \int dY_n \left[ \theta\left(\sum_{k=1}^n y_k\right) \left( \int_0^\infty e^{-y_{n+1}} dy_{n+1} + \int_{-\sum_{k=1}^n y_k}^0 dy_{n+1} \right) + \right. \\
&\quad \left. + \theta\left(-\sum_{k=1}^n y_k\right) \int_{-\sum_{k=1}^n y_k}^\infty e^{-y_{n+1}} dy_{n+1} \right] = \\
&= \int dY_n \left[ \theta\left(\sum_{k=1}^n y_k\right) \left(1 + \sum_{k=1}^n y_k\right) + \theta\left(-\sum_{k=1}^n y_k\right) e^{\sum_{k=1}^n y_k} \right] = 2O_n + nL_n . \quad (33)
\end{aligned}$$

For the linear term, we have two recursions, depending on whether we define the linear term by integrating  $y_1$  or  $y_{n+1}$  (these two integrals are equal due to permutation symmetry). Namely:

$$\begin{aligned}
L_{n+1} &= \int y_1 dY_{n+1} \theta\left(\sum_{k=1}^{n+1} y_k\right) = \int y_1 dY_n \left[ \theta\left(\sum_{k=1}^n y_k\right) \left(1 + \sum_{k=1}^n y_k\right) \right. \\
&\quad \left. + \theta\left(-\sum_{k=1}^n y_k\right) e^{\sum_{k=1}^n y_k} \right] = Q_n + (n-1)M_n = \frac{I_n}{n} \quad (34)
\end{aligned}$$

where we have defined

$$I_n := \int \left(\sum_{k=1}^n y_k\right)^2 dY_n \theta\left(\sum_{k=1}^n y_k\right) = nQ_n + n(n-1)M_n . \quad (35)$$

The last equation can be easily proved by expanding the square under the integral. By defining the linear term with the integration of  $y_{n+1}$ , we get:

$$\begin{aligned}
L_{n+1} &= \int y_{n+1} dY_{n+1} \theta \left( \sum_{k=1}^{n+1} y_k \right) = \\
&= \int dY_n \left[ \theta \left( \sum_{k=1}^n y_k \right) \left( 1 - \frac{1}{2} \left( \sum_{k=1}^n y_k \right)^2 \right) + \theta \left( - \sum_{k=1}^n y_k \right) \left( 1 - \sum_{k=1}^n y_k \right) e^{\sum_{k=1}^n y_k} \right] = \\
&= 2O_n - \frac{1}{2}I_n + nL_n . \quad (36)
\end{aligned}$$

Combining eqs. (33), (34) and (36), we get a system of coupled recursive relations:

$$\begin{cases} O_{n+1} = 2O_n + nL_n , \\ L_{n+1} = \frac{I_n}{n} , \\ L_{n+1} = 2O_n - \frac{I_n}{2} + nL_n , \end{cases} \quad (37)$$

which easily gives a relation between the linear and zeroth order term as  $(n+1)L_n = 2O_n$ . Moreover, we can easily solve for the linear term:

$$L_{n+1} = \frac{2(n+1)}{n+2} L_n , \quad (38)$$

which is the same recursion satisfied by  $c_n$ . Since  $L_1 = 1$ , we obtain

$$\begin{cases} L_n = c_{n-1} , \\ I_n = nc_n , \\ O_n = \frac{n+1}{2} c_{n-1} . \end{cases} \quad (39)$$

To complete the proof, we have to show that  $I_n = Q_n$ . This, together with eq. (39), would imply that  $Q_n = nc_n$  and  $M_n = -c_n$ , which are equivalent to eq. (22). Let us consider the integration over  $y_{n+1}$ :

$$\begin{aligned}
I_{n+1} &= \int \left( \sum_{k=1}^{n+1} y_k \right)^2 dY_{n+1} \theta \left( \sum_{k=1}^{n+1} y_k \right) \\
&= \int \left[ y_{n+1}^2 + \left( \sum_{k=1}^n y_k \right)^2 + 2y_{n+1} \left( \sum_{k=1}^n y_k \right) \right] dY_{n+1} \\
&= Q_{n+1} + \int \left( \sum_{k=1}^n y_k \right)^2 dY_n \left[ \theta \left( \sum_{k=1}^n y_k \right) \left( 1 + \sum_{k=1}^n y_k \right) + \theta \left( - \sum_{k=1}^n y_k \right) e^{\sum_{k=1}^n y_k} \right] + \\
&\quad + \int 2 \left( \sum_{k=1}^n y_k \right) dY_n \left[ \theta \left( \sum_{k=1}^n y_k \right) \left( 1 - \frac{1}{2} \left( \sum_{k=1}^n y_k \right)^2 \right) + \right. \\
&\quad \left. + \theta \left( - \sum_{k=1}^n y_k \right) e^{\sum_{k=1}^n y_k} \left( - \sum_{k=1}^n y_k + 1 \right) \right] = Q_{n+1} , \quad (40)
\end{aligned}$$

for all  $n$  integers. This completes the proof.

## B Additional information on the benchmark tasks

### B.1 Benchmark models

#### B.1.1 Hyperboloid

The hyperboloid model (Forbes et al., 2022) is a 2-component mixture of tri-variate Student's  $t$ -distributions of the form

$$\begin{aligned}
\boldsymbol{\theta} &\sim \mathcal{U}_2(-2, 2) \\
\mathbf{s} \mid \boldsymbol{\theta} &\sim \frac{1}{2} t_3(\nu, F(\boldsymbol{\theta}; \mathbf{a}_1, \mathbf{a}_2) \mathbb{I}, \sigma^2 \mathbf{I}) + \frac{1}{2} t_3(\nu, F(\boldsymbol{\theta}; \mathbf{b}_1, \mathbf{b}_2) \mathbb{I}, \sigma^2 \mathbf{I}) ,
\end{aligned}$$

which are parameterized by degrees of freedom  $\nu$ , mean

$$F(\boldsymbol{\theta}; \mathbf{x}_1, \mathbf{x}_2) = \text{abs}(\|\boldsymbol{\theta} - \mathbf{x}_1\|_2 - \|\boldsymbol{\theta} - \mathbf{x}_2\|_2),$$

and scale matrix  $\sigma^2 \mathbf{I}$ .  $\mathbf{I}$  is a three-dimensional vector of ones. We follow Forbes et al. (2022) and set  $\mathbf{a}_1 = [-0.5, 0.0]^T$ ,  $\mathbf{a}_2 = [0.5, 0.0]^T$ ,  $\mathbf{b}_1 = [0.0, -0.5]^T$ ,  $\mathbf{b}_2 = [0.0, 0.5]^T$ ,  $\nu = 3$  and  $\sigma^2 = 0.01$  for our experiments. Hence, while the parameter vector  $\boldsymbol{\theta}$  is two-dimensional,  $\mathbf{s}$  has three dimensions.

### B.1.2 Gaussian mixture model

The Gaussian mixture (GMM) uses the following generative process:

$$\begin{aligned}\boldsymbol{\theta} &\sim \mathcal{U}_2(-10, 10) \\ \mathbf{s} \mid \boldsymbol{\theta} &\sim \frac{1}{2} \mathcal{N}_2(\boldsymbol{\theta}, \mathbf{I}) + \frac{1}{2} \mathcal{N}_2(\boldsymbol{\theta}, \sigma^2 \mathbf{I})\end{aligned}$$

where  $\sigma^2 = 0.01$ ,  $\mathbf{I}$  is a unit matrix, and both  $\boldsymbol{\theta} \in \mathbb{R}^2$  and  $\mathbf{s} \in \mathbb{R}^2$  are two-dimensional random variables. The GMM follows the representation in Lueckmann et al. (2021).

### B.1.3 Mixture model with distractors

We introduced a new benchmark model that, similarly to the SLCP task (Lueckmann et al., 2021), appends the data with dimensions that are not informative of the parameters. Specifically:

$$\begin{aligned}\theta &\sim \mathcal{U}(-10, 10) \\ s_1, s_2 &\sim \alpha \mathcal{N}(\theta, 1) + (1 - \alpha) \mathcal{N}(-\theta, \sigma^2) \\ s_3, \dots, s_{11} &\sim \mathcal{N}(0, 1),\end{aligned}\tag{41}$$

where we set  $\alpha = \sigma = 0.3$ . For each observation, the mixture model with distractors samples twice and independently from a mixture of Gaussians. In addition, 9 samples from a standard Gaussian are drawn which do not carry information of the parameters. If both  $s_{1,obs}$  and  $s_{2,obs}$  are from the same mode (in our experiments we set  $s_{1,obs} = s_{2,obs} = 5$ ), then the posterior for  $\theta$  is approximately bimodal with very uneven mass distribution among the two modes. Hence, it is a very challenging distribution to sample.

### B.1.4 Two moons

Two moons is a common benchmark task in the SBI literature. Its generative process is defined as:

$$\begin{aligned}\boldsymbol{\theta} &\sim \mathcal{U}_2(-10, 10) \\ \alpha &\sim \mathcal{U}(-\pi/2, \pi/2) \\ r &\sim \mathcal{N}(0.1, 0.01^2) \\ \mathbf{s} \mid \boldsymbol{\theta} &= \begin{pmatrix} r \cos \alpha + 0.25 \\ r \sin \alpha \end{pmatrix} + \begin{pmatrix} -|\theta_1 + \theta_2|/\sqrt{2} \\ -(\theta_1 + \theta_2)/\sqrt{2} \end{pmatrix},\end{aligned}$$

where we are interested in inferring the two-dimensional posterior  $p(\boldsymbol{\theta} \mid \mathbf{s})$  and treat  $\alpha$  and  $r$  as nuisance parameters.

## B.2 Experimental details

For the two moons and mixture model benchmark tasks, we used the reference posterior distributions of the `sbi` Python package (Tejero-Cantero et al., 2020). For the hyperboloid model and mixture model with distractors, we draw a posterior sample of size 100 000 using a slice sampler using the `sbijax` Python package (Dirmeier et al., 2024). We sample 10 independent chains of length 20 000 of which the first 10 000 samples are discarded as warm-up. We then pool the samples of all 10 chains. We used conventional MCMC sampler diagnostics (i.e., potential scale reduction factor and effective sample size) to monitor convergence.

We compare the inferred posterior distributions to the reference posterior distributions using C2ST (Lopez-Paz and Oquab, 2017), MMD (Sutherland et al., 2017) and H-Min (Zhao et al., 2022) metrics. All metrics are computing by subsampling 10 000 posterior samples without replacement from the inferred posterior and reference posterior distributions.

Conversely to the previous literature which evaluated their methods with only few simulations (e.g., up to 10 000), we simulate data such that each method is trained to optimality. Since all our benchmarks are very low-dimensional, we trained each neural SBI method with  $N = 250\,000$  simulated model outputs (we evaluated training each method using 500 000 model outputs using two different random seeds, but found no inferential difference between 250 000 and 500 000 samples). For sampling-based methods, i.e., SMCABC and SABC, we evaluated 50 million population updates of an initial population of 10 000 particles. While we did not conduct exhaustive experiments, we observed that much smaller number of population updates (i.e, 10 - 20 million) yielded comparable performance for both SMCABC and all SABC variants. Details for each method are shown below. If not noted otherwise, all neural methods use an Adam optimizer using a learning rate of  $l = 0.0001$  and are trained to convergence with a maximum of 2 000 iterations.

Each experiment was run on an AMD EPYC™ 7742 processor with 64 cores and 256 GB RAM. Runtimes have not been thoroughly monitored but lay between 2-8h. In total we computed 140 experiments (5 seeds times 6 experimental models times 4 benchmark tasks). We use the workflow tool Snakemake (Köster and Rahmann, 2012) to run all experiments automatically on a Slurm cluster.

**SABC** SABC has only few tuning parameters and proves to be quite robust w.r.t. their choice. For all cases in this paper, we use the standard choices: The annealing speed is set to  $v = 1$ . An importance sampling step decreasing the temperature by a factor  $1 + \delta = 1.1$  is performed every  $2 \times (\text{number of particles})$  successful updates. For the jumps in parameter space we replaced the original normal jump distribution by an interacting particle mechanism Ter Braak (2006); Goodman and Weare (2010). For all experiments, we used an Euclidean distance function as a metric. The code has been released as a Julia package: <https://github.com/Eawag-SIAM/SimulatedAnnealingABC.jl>

**SMC-ABC** For SMC-ABC, we set the  $\epsilon$ -decay to 0.9 finding that this gave the best results for the number of population updates (50 million). We resample the population when the relative effective sample size is below 0.2 which we empirically found to work well. As before, we use a Euclidean distance function.

**APT** APT uses a neural spline flow (Durkan et al., 2019) consisting of 5 normalizing flow layers. The flow uses a residual network with 10 bins, 2 blocks, and 64 hidden nodes per block.

**BNRE** BNRE uses a residual network as a classifier using 5 blocks of 64 hidden nodes each.

**FMPE** FMPE uses a residual network as a score network which consists of 5 blocks of 64 hidden nodes each. We used a time-embedding dimensionality of 32.

**NPSE** Since FMPE and NPSE are algorithmically identical and only differ in the definition of the forward process (see, e.g., Tong et al. (2024)), we chose to use a MLP using 5 layers with 64 hidden nodes each for NPSE expecting otherwise very similar results to FMPE (we note that this is the same architecture as in the original publication (Sharrock et al., 2024)). We used the variance-preserving SDE and a time-embedding dimensionality of 32.



## B.3 Additional results

### B.3.1 Full table of results

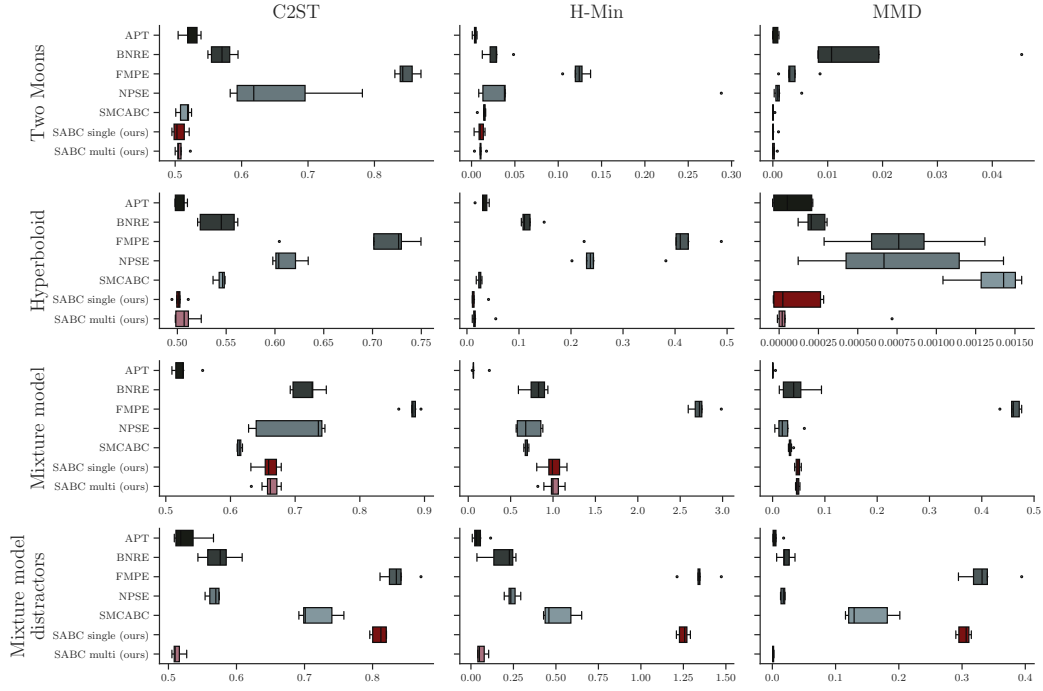


Figure 6: Evaluation of SABC and baseline methods on benchmark tasks using C2ST, H-min, and MMD metrics.

### B.3.2 Posterior distributions

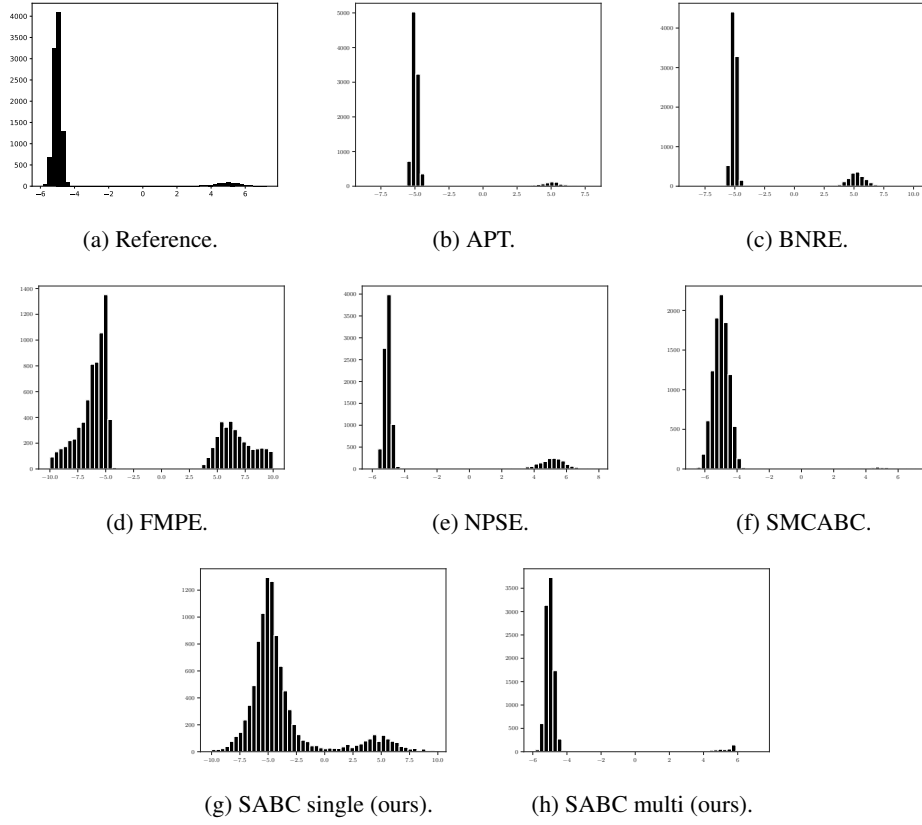


Figure 7: Posterior distributions for the mixture model with distractors example using a specific seed.

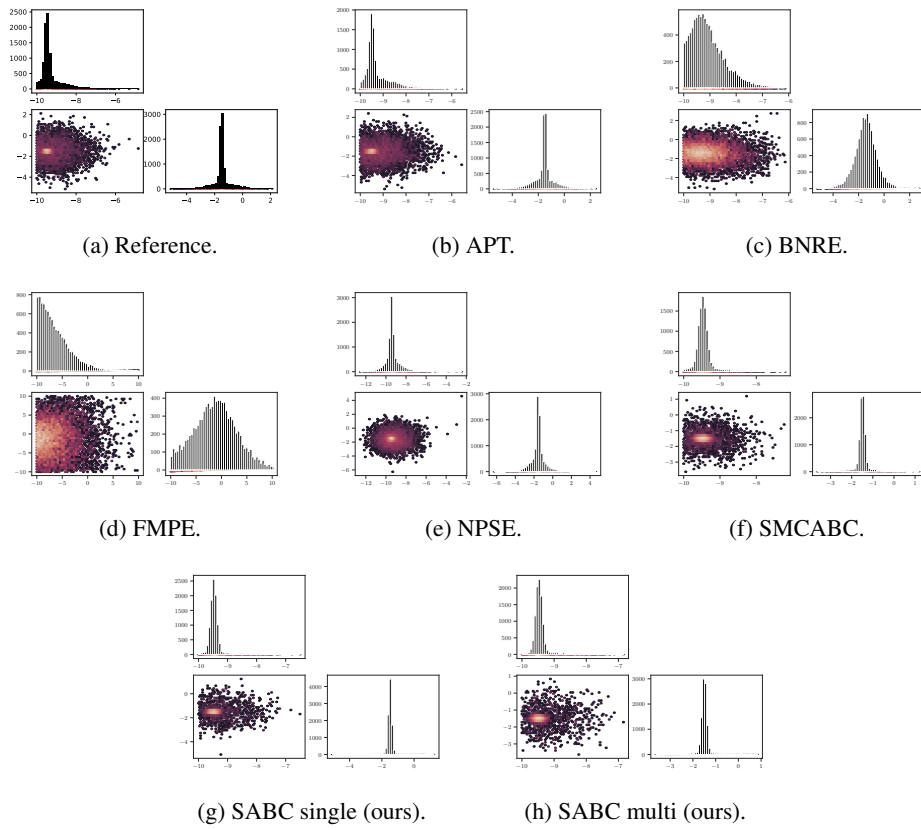


Figure 8: Posterior distributions for the mixture model example using a specific seed.

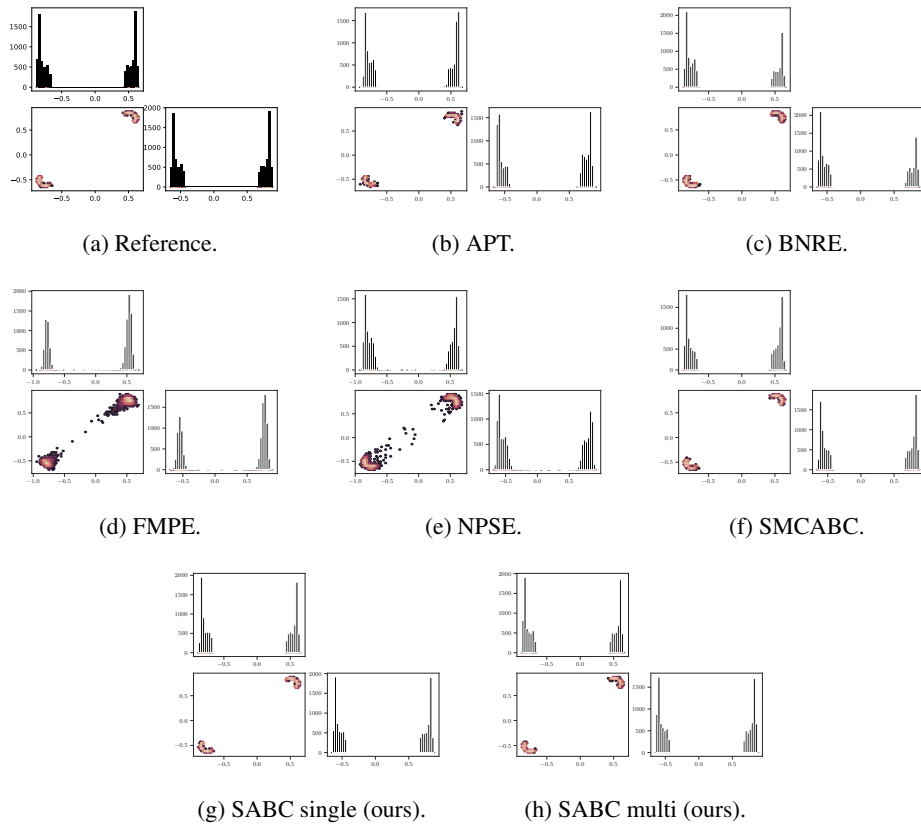


Figure 9: Posterior distributions for the two moons example using a specific seed.

### B.3.3 Rho trajectories

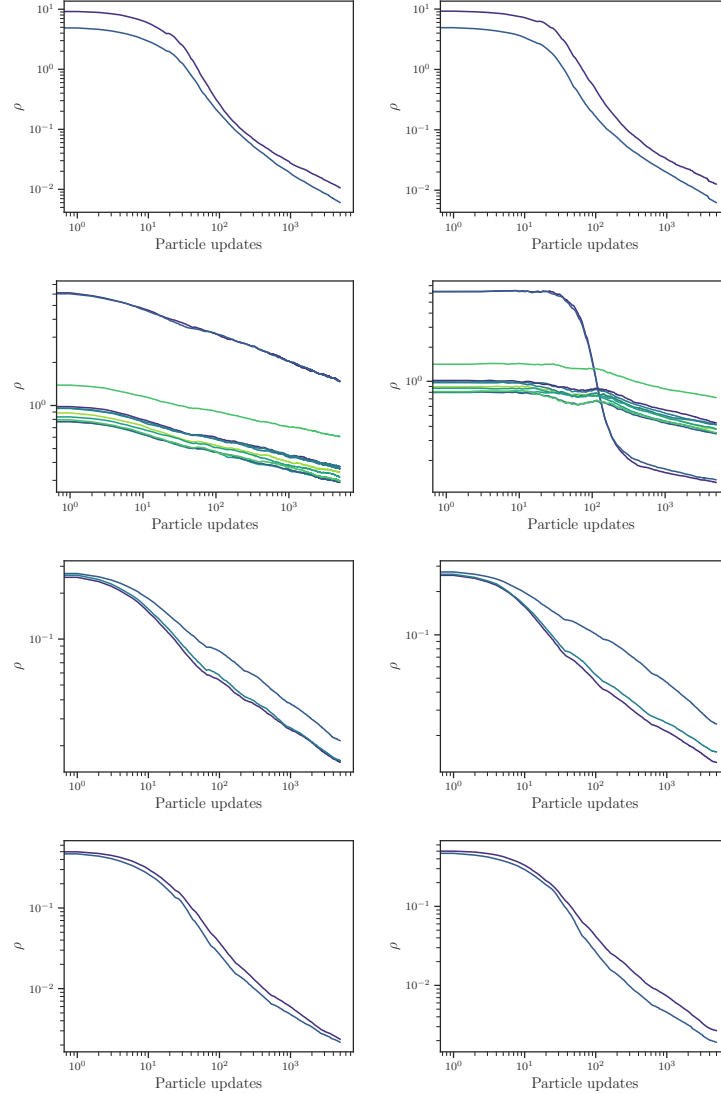


Figure 10: Trajectories of individual distances  $\rho_i$  during SABC sampling. From top to bottom, we show results from the mixture model, the mixture model with distractors, the hyperboloid and two moons examples. The left column shows SABC with a single temperature and the right one with multiple temperatures. Using a single temperature tends to keep the distances to the individual summary statistics closer together. On the other hand, using multiple temperatures can allow more informative statistics to converge faster, as is the case for the model with distractors (second row).

## C Additional information on the solar dynamo model

### C.1 Model description

We consider a second-order stochastic delay differential equation model describing the time evolution of the solar magnetic field strength  $B(t)$  (Wilmot-Smith et al., 2006; Albert et al., 2021):

$$\left(\tau \frac{d}{dt} + 1\right)^2 B(t) = -\mathcal{N}_d F(B(t-T)) + \sqrt{\tau} B_{\max} \sigma \eta(t), \quad (42)$$

where  $\tau$  is the magnetic diffusion timescale,  $\mathcal{N}_d$  is the dimensionless dynamo number, quantifying the efficiency of the field-generating dynamo process, which amplifies and sustains magnetic fields against field-destroying diffusive decay in the solar interior,  $T$  is a time-delay parameter accounting for the finite timescales associated with the transport of magnetic fields by meridional circulation and the buoyant rise of magnetic flux tubes through the solar convection zone, and

$$F(B) = \frac{B}{4} (1 + \operatorname{erf}(B^2 - B_{\min}^2)) (1 - \operatorname{erf}(B^2 - B_{\max}^2)), \quad (43)$$

is a nonlinear quenching function that restricts the action of the field-generating mechanisms to field strengths in the range  $B_{\min} \lesssim B \lesssim B_{\max}$ . The last term on the right-hand side of Equation (42) is an additive white-noise contribution, with  $\langle \eta(t)\eta(t') \rangle = \delta(t-t')$  and standard deviation  $\sqrt{\tau} B_{\max} \sigma$ . Here  $\sigma$  is the dimensionless noise amplitude. For further details on the model and its parameters, see Albert et al. (2021) and references therein. The vector of parameters to be inferred is  $\theta = \{B_{\max}, \mathcal{N}_d, T, \sigma, \tau\}$  for which we use the following prior distributions

$$\begin{aligned} B_{\max} &\sim \mathcal{U}(1.0, 15.0), \\ \mathcal{N}_d &\sim \mathcal{U}(1.0, 15.0), \\ T &\sim \mathcal{U}(0.1, 120), \\ \sigma &\sim \mathcal{U}(0.01, 0.3), \\ \tau &\sim \mathcal{U}(0.1, 120). \end{aligned}$$

The lower threshold  $B_{\min}$  is not inferred and is set to  $B_{\min} = 1$ .

We use the official monthly mean SN record from Clette and Lefèvre (2015), which consists of 3251 observations covering the time span 1749-2019. We assume that the observed SN values are proportional to the squared magnetic field  $B^2(t)$ . Observations  $\mathbf{x}_{obs}$  are sampled at  $N+1$  time points  $n\Delta t$ , with  $n = 0, 1, \dots, N$ , and with the sampling interval  $\Delta t = 1$  month. In the SABC inference we compare the summary statistics  $\mathbf{s}_{obs}$  to the corresponding features  $\mathbf{s} = \mathbf{s}(\mathbf{x})$  where  $\mathbf{x} = \mathbf{B}^2$  and  $\mathbf{B}$  is the model output sampled at the same  $N+1$  time points as the observed data. The comparison is made using a standard Euclidean distance between the individual summary statistics.

Given the oscillatory nature of the system, it is convenient to focus on specific spectral features of the data. Therefore, we consider selected Fast Fourier Transform (FFT) components as summary statistics. However, applying the FFT requires windowing the data to reduce spectral leakage. We use the discrete Hann window, a well-established method in signal processing,

$$w_n = \sin^2\left(\frac{\pi n}{N}\right), \quad 0 \leq n \leq N. \quad (44)$$

It can be shown that the Hann window introduces correlations between Fourier modes whose index difference is less than 3. Here we adopt the absolute values of 20 FFT components with indexes varying in steps of 6, that is,  $\{0, 6, 12, 18, 24, \dots, 114\}$ , as summary statistics. This choice allows us to avoid the correlations between Fourier modes introduced by the Hann window, while retaining enough information to characterize the spectral properties of the data. Moreover, ignoring higher-order modes allows us to discard high-frequency noise that may not be adequately captured by the model. For more information, see Ulzega et al. (2025).

### C.2 Experimental details

For the solar dynamo model, we evaluated the SABC (single) version against the sequential neural SBI methods SNLE Papamakarios et al. (2019) and APT Greenberg et al. (2019). We also conducted

extensive experiments using SNLE, APT, FMPE, NPSE, and the dimensionality-reducing SSNLE (Dirmeier et al., 2023) on the raw solar dynamo data, but found that a) using manually crafted summary statistics works better than evaluating the aforementioned methods on the raw data, and b) that SNLE and APT produced significantly better posterior inferences than the other previously used baselines (data not shown).

For both APT and SNLE, we use masked autoregressive flows with 10 flow layers (Papamakarios et al., 2017). Each flow layer uses an autoregressive network with 2 layers and 64 hidden nodes. Both APT and SNLE are trained sequentially for 10 rounds, where for each round we generate 20 000 novel outputs using the proposal posteriors obtained from the previous round. We use slice samplers for both APT and SNLE to draw samples from the proposal posterior distributions. We use an Adam optimizer with a learning rate of 0.0001 and train until convergence or until 2 000 iterations are reached, respectively. After the last round of training, we draw a posterior sample of size 20 000 which we then use to draw 20 000 realizations from the PPD (eq. 21) (i.e., one draw for each posterior sample).

For SABC, we have opted for the yearly mean SN dataset (Clette and Lefèvre, 2015) over the higher-resolution monthly mean SN, as it retains sufficient resolution to capture the spectral features of interest while substantially reducing the high computational cost typical of ABC-type algorithms. The yearly SN dataset comprises 271 data points. We have initially run the inference using 10 000 particles. Then, to refine the posterior sample, we have performed a final importance sampling step by discarding slowly converging, less informative particles with the largest distances between observed and simulated data. To this end, we impose an arbitrary cut-off distance such that the least well-converged 30% of the particles are removed from the posterior sample. The latter thus consists of about 7000 particles. The hyperparameters are the same as the benchmark tasks.

For visualization (i.e., Figure 5), we sort the PPD samples by their Euclidean distance to the observed summary statistics  $s(\mathbf{x}_{obs})$  and take 50 samples corresponding to equidistantly-spaced quantiles of the distances.

The SNLE and APT experiments were conducted on an AMD EPYCTM 7742 processor with 64 cores and 256 GB RAM. Runtimes were roughly 24 hours in both cases. The SABC algorithm was run on a single HPE ProLiant XL230k Gen10 node using 32 Xeon-Gold 6142 2.6GHz processors with 196 GB of RAM. The full inference, with  $5 \cdot 10^8$  particle updates, required about 120 hours.

### C.3 Additional results

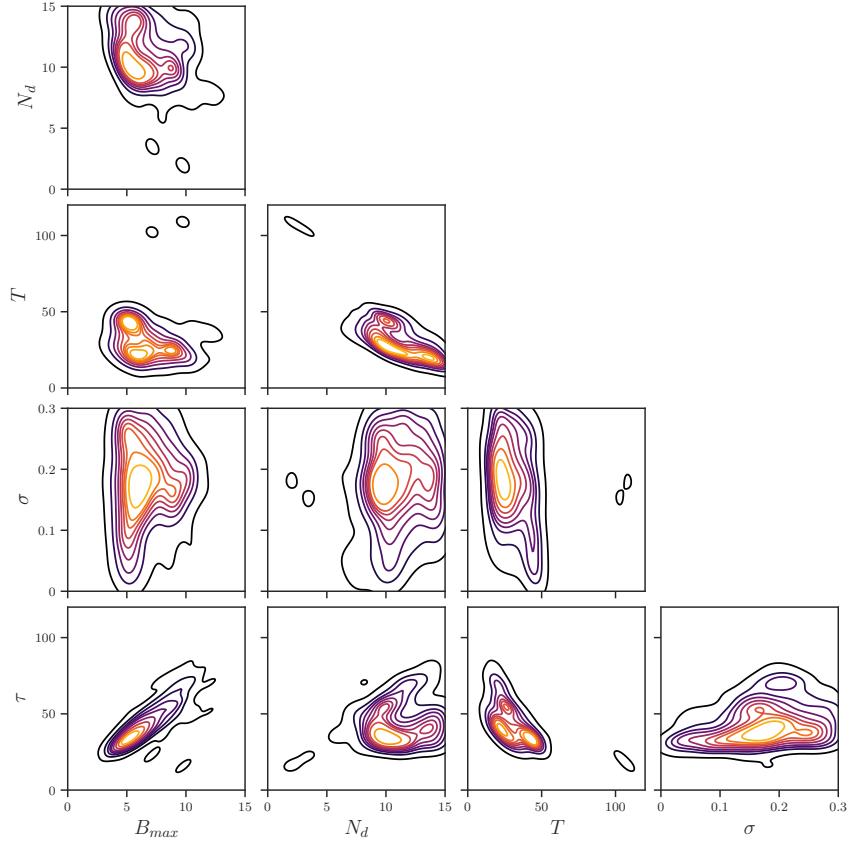


Figure 11: SABC bivariate densities.



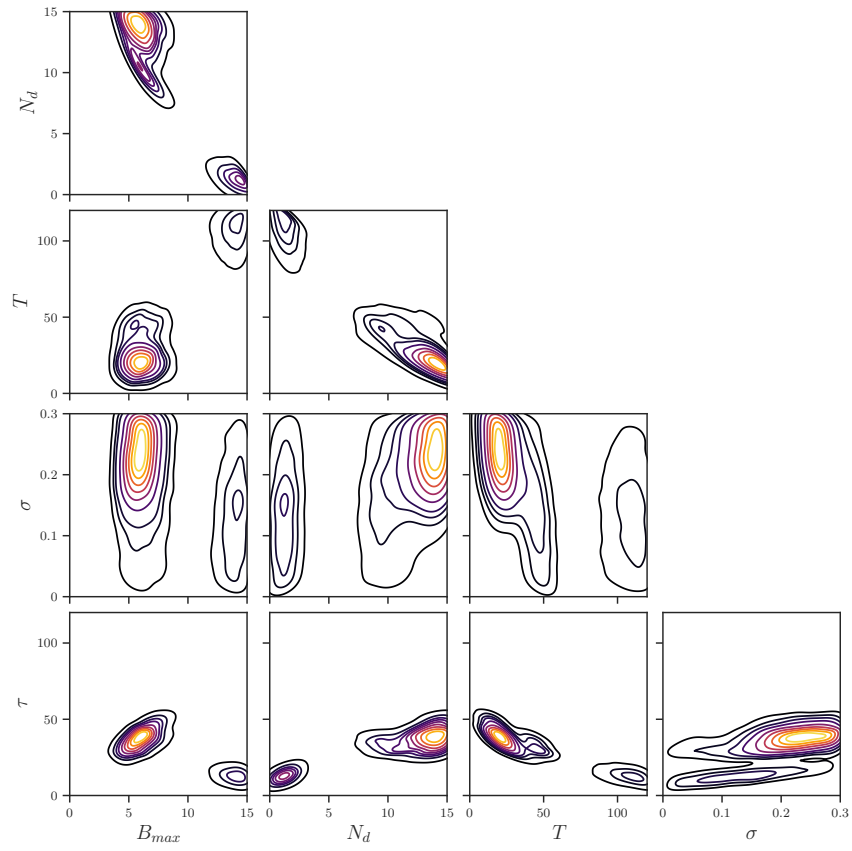


Figure 12: Sequential APT bivariate densities after 10 rounds.

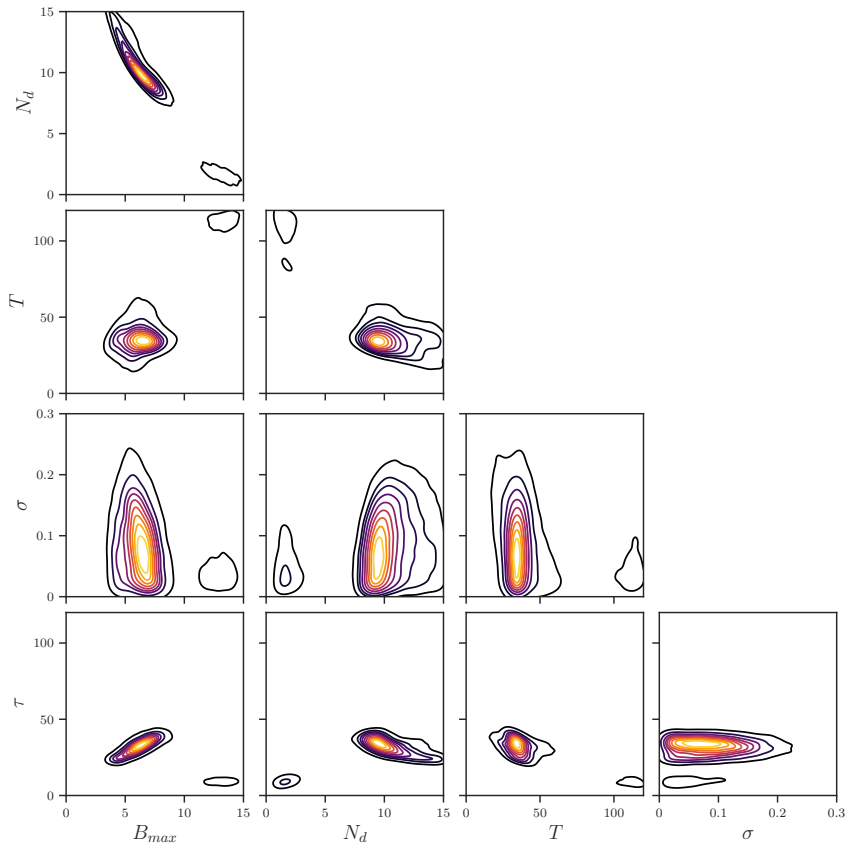


Figure 13: Sequential NLE bivariate densities after 10 rounds.

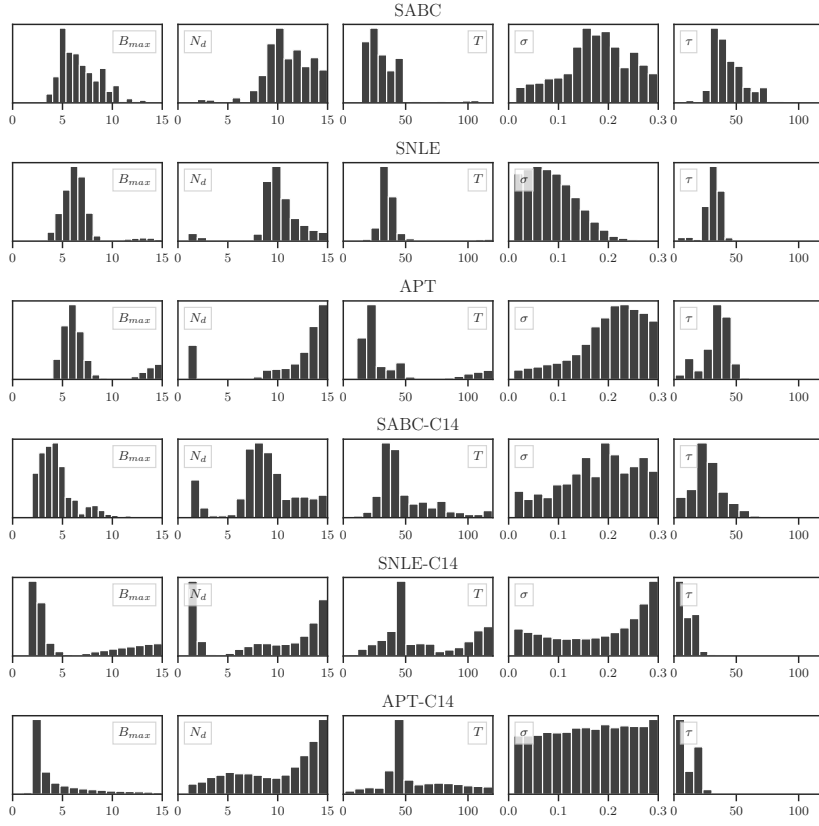


Figure 14: Marginal distributions of the posterior of SABC, SNLE and APT for the sun spots (top three rows) and  $^{14}\text{C}$  (bottom three rows), respectively.

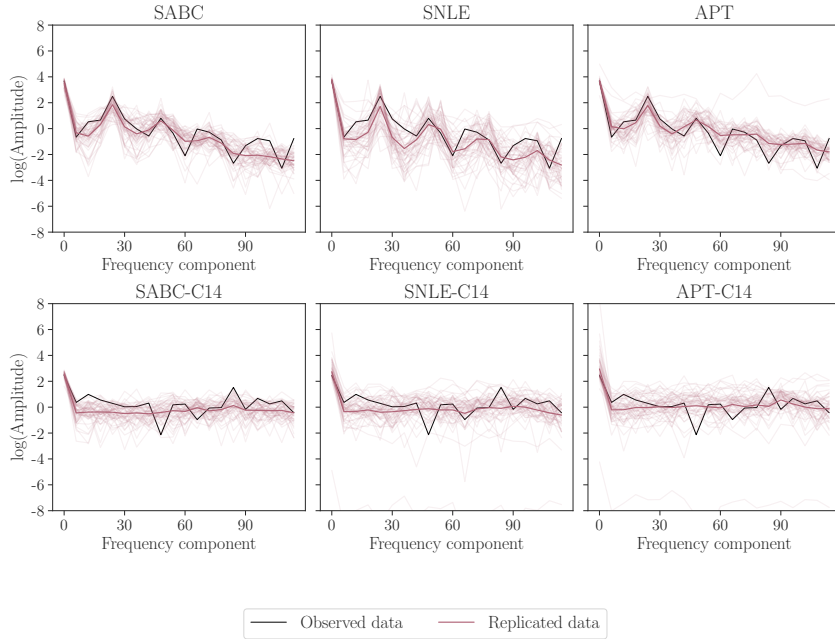


Figure 15: Posterior predictive distributions of SABC, SNLE and APT, for the sun spots (top row) and  $^{14}\text{C}$  (bottom row), respectively.

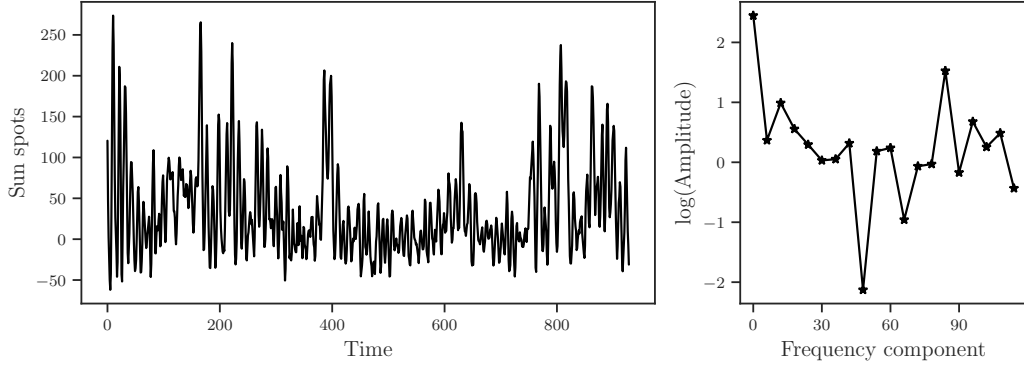


Figure 16:  $^{14}\text{C}$  data and the 20 FFT components used for posterior inference.

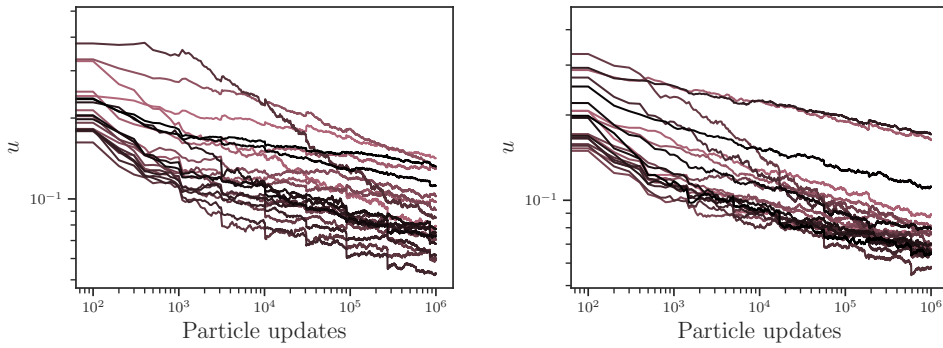


Figure 17: Convergence of energies ( $u$ 's) of SABC for sunspots (left) and  $^{14}\text{C}$  (right). The colors represent the different summary statistics (i.e., the 20 FFT components).